The Effects of Defects on Tensile Properties of Cast ADC12 Aluminum Alloy

MITSUHIRO OKAYASU and HIKOYUKI SAKAI

To better understand the effects of cast defects on mechanical properties, cast aluminum alloys with various porosities were used. Porosity in the cast samples was created during the casting process, and to clearly identify the porosity effects on the mechanical properties, artificial defects (porosity-like tiny holes) were created mechanically. The tensile properties for the cast aluminum alloys appear to be attributed to the area fraction of the porosity on the fracture surface (namely, the defect rate, DR), although there were different trends because of the different stress concentrations: the ultimate tensile strength and 0.2 pct proof strength were linearly related to DR, while a non-linear correlation was detected for fracture strain. Even in Al alloys with small amounts of defects, significant reductions in the fracture strain were observed. These results were verified using tensile tests on specimens containing artificial defects. The effects of artificial defects on the tensile properties were further investigated using numerous tiny holes, created in several formations. The artificial defects (several small holes), lined up at perpendicular (90 deg) and 45 deg directions against the loading direction, made significant reductions in the tensile properties, even though only weak defect effects were observed for the 90 deg loading direction. No severe defect effects were obvious for the specimen with a tiny defect of ϕ0.1 mm, because of the lower stress concentration, compared to the microstructural effects in the cast Al alloys: the grain boundaries and the second phases. Such phenomena were clarified using tensile tests on cast samples with differently sized microstructures. There were no clear defect effects on the yield strength as the defect amount was less than 10 pct, and microstructural effects were not detected either in this case. Failure characteristics during tensile loading were revealed directly by *in-situ* strain observations using high-speed cameras.

© The Minerals, Metals & Materials Society and ASM International 2015

I. INTRODUCTION

In the automotive industry, aluminum alloys are the optimum choice for the manufacture of parts, because of their low weight and for environmental reasons, especially lower fuel consumption[1] and lower CO_2 emission.[2] In fact, automotive parts made of cast irons (γ = 7.8 g/cm^3) have been replaced with lighter aluminum alloys (γ = 2.7 g/cm^3), and the production of cast aluminum alloy for automotive parts has increased in recent years.[2] The advantages of cast Al alloys include not only their light weight, with a density of approximately one third that of cast iron, but also their attractive appearance, excellent fabricability, and high resistance to corrosion.[3] In particular, the use of aluminum-silicon-copper (Al-Si-Cu) cast alloys is widespread in different fields of application because of their good castability. However, cast Al-Si-Cu components possess complicated

microstructures and exhibit various defects, so the use of cast Al alloys to replace cast iron in the manufacture of safety-critical parts in automobiles is significantly restricted because of their low mechanical properties or low reliability. The mechanical properties of cast Al alloys have been investigated, and it was found that failure (or crack initiation) occurred, originating from the cast defects. One of the significant defects was associated with porosity (*i.e.*, blow holes),[4,5] because related defects could involve the cast sample, especially caused by pressure casting, *e.g.*, the cold-chamber die casting process. Jana *et al.*[6] reported that fatigue cracks emanated from the edges of porosities as a result of high stress concentration. There was a strong correlation between the porosity and mechanical properties of the cast Al alloys, in which the parameter of global volumetric porosity was used.[7] In the study by Zhao *et al.*,[8] the tensile properties of Al-Si-Cu cast plate samples were found to be directly affected by porosity. The effects of porosity on mechanical properties have been investigated by several researchers (*e.g.*,[9]). Irfan *et al.*[1] reported that there was a linear correlation between the pore area and ultimate tensile strength, but their data appeared to be slightly scattered. They stated that "due to the scatter in data it is hard to make any meaningful conclusions based on this data." In their approach, the pore area was determined on one particular section of the tensile test sample, which may not be representative of the whole

MITSUHIRO OKAYASU, Professor, is with Graduate School of Natural Science and Technology, Okayama University, 3-1-1 Tsushima-naka, Kita-ku, Okayama, 700-8530, Japan. Contact e-mails: mitsuhiro. okayasu@utoronto.ca, okayasu@okayama-u.ac.jp HIKOYUKI SAKAI, Master Student, is with the Department of Materials Science and Engineering, Graduate School of Science and Engineering, Ehime University, 3 Bunkyo-cho, Matsuyama, Ehime 790-8577, Japan.
Manuscript submitted January 19, 2015.
Article published online September 8, 2015.

volume of the tensile sample. Weiler and Wood[10] carried out an examination of the relationship between the fracture strain (ε_f) and the area fraction of the porosity (f) using finite element (FE) analysis. In their work, a centered pore model was employed, where the model was characterized by an empirical relationship: $\varepsilon_f = 0.016f^{-0.30}$. Their prediction was in good agreement with the fracture strains resulting from the failure model discussed in Reference 11. Several investigators have examined the influences of defects on the tensile properties in cast Al alloys experimentally and theoretically. Cáceres and Selling[12] have examined the relationship between the casting defects and tensile properties for an Al-Si-Mg alloy, where it appears that the decrease in tensile properties correlates with the area fraction of defects in the fracture surface of the samples, and their experimental results are in agreement with the prediction of a simple analysis based upon models for the growth of a plastic instability in a tensile sample.[12] The influence of the porosity on the fatigue behavior of Al-Si-based aluminum alloys has been investigated experimentally.[3,13] The porosity was observed to have the greatest propensity for acting as a crack initiation site, and the fatigue strength decreased when the size of the porosity increased.[3] Several investigators have examined the influences of defects on the mechanical properties in cast Al alloys. However, the authors believe that there is still a lack of experimental data to clearly understand them. This is because detailed defect information, *i.e.*, defect size, shape, and position, has not been considered. We also have to consider that the mechanical properties of cast aluminum alloys (Al-Si-Cu) are affected not only by the defects, but also by their complicated microstructures (coarse α-Al phase and needle-shaped eutectic phases).[14]

Thus, in the present work, the mechanical properties of cast Al-Si-Cu alloys were examined using specimens with various defects: (i) porosity (created in the casting process) and (ii) porosity-like tiny holes (artificial defects). The artificial defects were made in various formations in cast samples without any cast defects.

II. EXPERIMENTAL PROCEDURES

A. *Material Preparation*

In this study, an Al-Si-Cu aluminum alloy (JIS-ADC12) was selected. The main chemical composition of this aluminum alloy was (mass pct): 10.6Si, 2.5Cu, 0.3Mg, 0.5Zn, 1.1Fe, 0.3Mn, 0.1Ni, and the remainder consisted of Al. The Al alloy samples were prepared by three different casting methods: (i) high-speed vacuumed casting (VC), (ii) heated mold continuous casting (HMC), and (iii) gravity casting (GC). The three different casting processes made cast samples with different amounts of porosity and different C.

The VC samples had fine microstructures, the HMC samples had fine microstructures, and the GC samples had coarse microstructures. HMC and GC samples did not have cast defects, including porosity, which was verified by X-ray diffraction. To clearly examine the effects of the defects on the mechanical properties of the cast Al alloys, artificial defects (porosity-like holes) were made directly into the HMC and GC specimens using tiny drills. Figure 1 presents schematic illustrations of the HMC and GC specimens ($8 \times 2 \times 1$ mm^3) with the artificial defects (tiny holes). The diameters of the tiny holes were determined to be from $\phi 0.1$ mm to $\phi 1$ mm (Figure 1(b)). Note that, in this approach, the small specimens were used due to the following reasons: (i) technical issue to make tiny holes (1 mm is the maximum specimen thickness to make $\phi 0.1$ mm hole); (ii) elimination of the cast defects from the specimen (stochastic). The number of artificial defects was changed from one to four. The artificial defects were created with different formations at 0, 45, and 90 deg directions against the loading direction (see Figure 1(c)). To prevent the microstructural change (grain growth and plastic deformation) during the machining process, the tiny holes were made at high rotation speed in machine oil. Because natural defects (porosity) were not clarified for HMC and GC by X-ray diffraction, we believe that artificial defects (tiny holes) would be the main defect in those specimens.

In the VC process, 15 g of the Al alloy was melted in an arc melter under vacuum at approximately 2.5×10^{-3} Pa, and injected rapidly into a copper mold using a vacuumed casting system designed by Makabe Giken Co., Ltd. A bulk Al alloy rod of dimensions ϕ 6 mm $\times$ 100 mm was fabricated at various injection speeds (casting speed, CS) of 400, 700, 1000, and 1300 mm/s. The reason for the different casting speeds was to make different volume fractions of porosity in the cast samples, where the extent of turbulent flow of the melt Al alloy during the injection process was altered.

In the HMC process, a horizontal-type HMC arrangement was used, which consisted of a melting furnace, a graphite crucible, a graphite mold, a cooling device, and a stainless steel dummy rod made for withdrawal of the cast sample. The size of the cast sample was 5 mm in diameter. Approximately, 200 g of ADC12 ingot was melted in the graphite crucible. The molten metal and mold were heated to just above the liquidus temperature of the ADC12 alloy. The melt Al alloy in the crucible was fed continuously into the mold at 1.9 mm/s under an argon gas atmosphere. The sample was water cooled just outside of the mold, where the liquid (or semi-solid) Al alloy rod of 5-mm diameter was solidified directly by water droplets.

In the GC process, the melt was poured directly into a metal mold ($600 \times 90 \times 40$ mm^3) for creating 5 kg metal ingots using a ladle. It should be noted that our GC process was not a representative conventional GC process, because our GC system did not have a sprue, runner, or gate.

B. *Experimental Details*

Tensile tests were conducted at room temperature using an electro-servo-hydraulic system with 50 kN load capacity. The relationship between the tensile stress and tensile strain was obtained using a standard load cell and strain gage. In the tensile tests, static tensile loading was conducted at 1 mm/min to final fracture. The strain
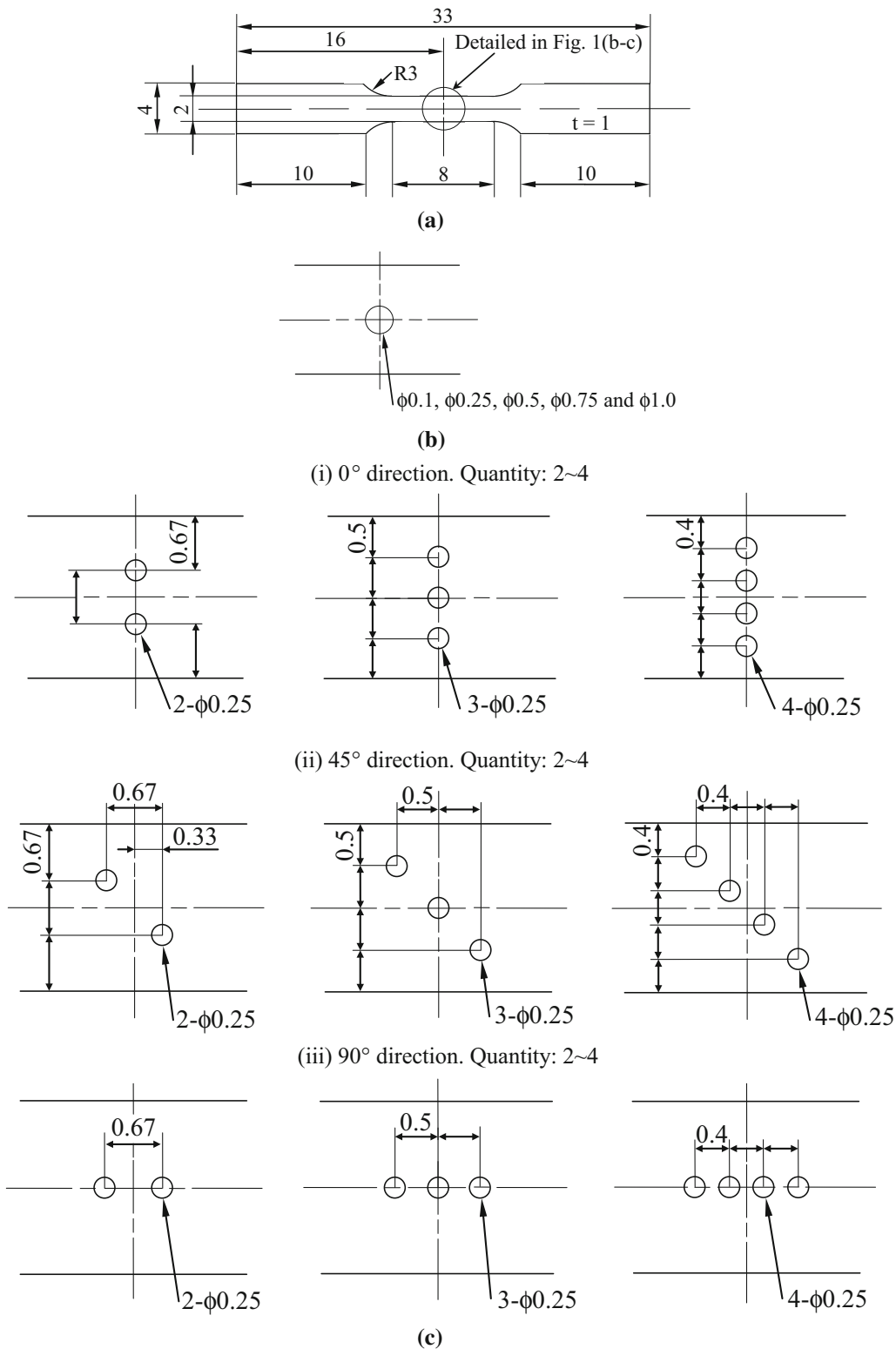
(a)

(b)

$\phi 0.1$, $\phi 0.25$, $\phi 0.5$, $\phi 0.75$ and $\phi 1.0$

(i) 0° direction. Quantity: 2~4

(ii) 45° direction. Quantity: 2~4

(iii) 90° direction. Quantity: 2~4

(c)

Fig. 1—Schematic illustrations of the test specimens with artificial defects. (*a*) Dumbbell shaped rectangular specimen. (*b*) Single hole with different diameters. (*c*) Several holes lined up with different formation.

characteristics were further examined experimentally and numerically using the following two methods: (i) a high-speed camera system and (ii) FE analysis. Figure 2 shows the experimental setup of the high-speed camera system, in which the two cameras (Photron FASTCAM-SA1.1) with related software for three-dimensional strain measurement (Correlation System VIC-2D, Correlated Solutions Inc.) were used. The strain level on the specimens was captured with an image resolution of 1024 × 1024 pixels at a frame rate of 5 kHz.

FE analysis was conducted to investigate the strain characteristics for the tensile test samples. In this analysis, two-dimensional FE simulation with eight-node quad elements was used. The models for the cast Al alloy were designed by considering the different microstructural phases, *e.g.*, α-Al, Cu, Si, and Fe. In this case, all eutectic phases for HMC samples (Cu, Si, and Fe) were considered to be combined as a colony in the FE analysis, because those phases are all fine and are mixed together. Such microstructural characteristics are demonstrated in section III–A. The material properties of the eutectic phase were determined on the basis of the applied load *vs* deformation relationships, measured using a dynamic ultra-micro-hardness tester (DUH-211 Shimadzu).[15,16] This tester can measure the mechanical properties in a small region on the specimen surface. Because of the greater hardness of the eutectic phase compared to the Al matrix phase, arising from the hard
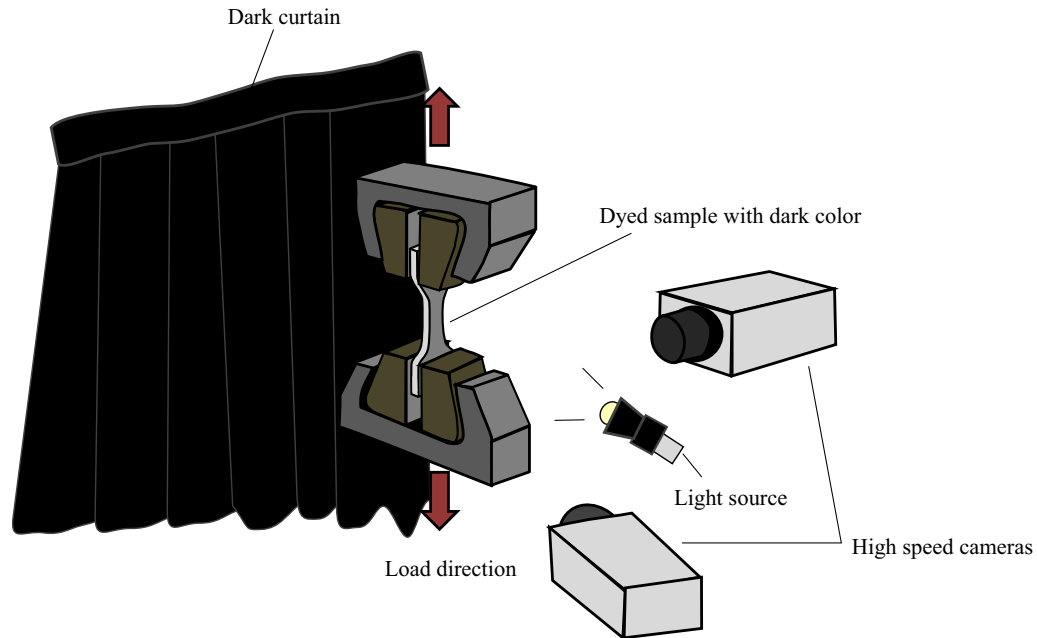

Fig. 2—Schematic diagram of the experimental setup for strain observation with high-speed cameras.

Table I. Material Properties of the HMC Samples for FE Analysis

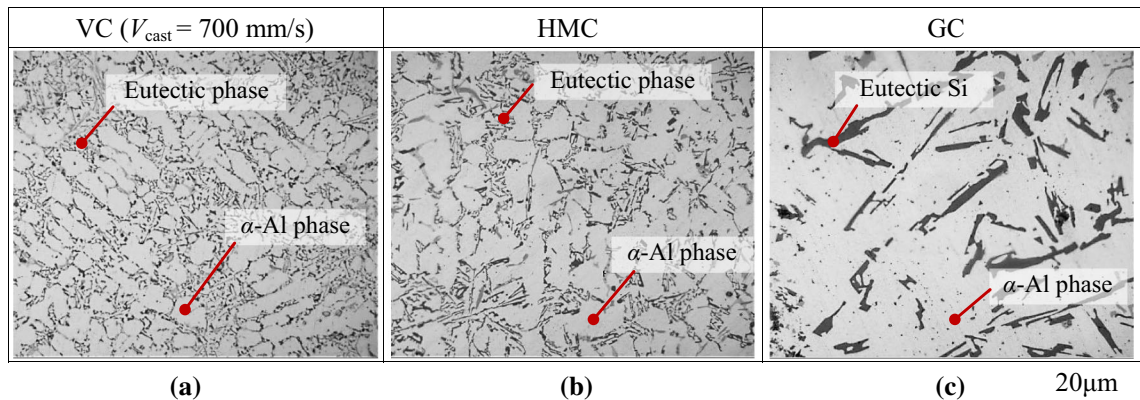|	HMC Sample	
	α-Al	Eutectic Phase
Young's modulus (GPa)	72.0	88.8
Tangent modulus (GPa)	7.2	8.9
Poisson's ratio	0.33	0.3

Fig. 3—Optical micrographs of cast ADC12 Al alloys: (*a*) VC, (*b*) HMC, and (*c*) GC samples.

Fe- and Si-based structures, the Poisson ratio for the eutectic phase was determined to be 0.3, while that for Al matrix was 0.33. To determine the plastic strain characteristics, the case of bilinear kinematics hardening was selected. In this case, the initial slope of the stress–strain curve was taken to be the elastic constant of the associated materials, and, after yielding, the stress–strain curve continued along a second slope, defined as the tangent modulus. The tangent modulus for each structure was determined to be equal to 10 pct of the elastic constant, as a first approximation. The material properties are summarized in Table I.

III. RESULTS AND DISCUSSION

A. Microstructural Characteristics

Figure 3 shows optical micrographs demonstrating the microstructures of the VC, HMC, and GC samples. Note that the microstructure of VC samples was only for the sample produced at 700 mm/s, because there were no clear microstructural differences between all VC samples, *i.e.*, at 400, 700, 1000, and 1300 mm/s casting speeds (CS). From Figure 3, fine and round α-Al phases with tiny eutectic structures consisting of Si, Fe, and Cu were obtained similarly for VC and HMC samples. This is because of the rapid solidification of the Al alloy. The secondary dendrite arm spacings (SDASs) for VC and HMC samples were found to be approximately 5.3 and 8.4 μm, respectively. On the other hand, large α-Al grains and needle-shaped eutectic structures were seen in the GC samples, where SDAS = 31.8 μm, because of the lower cooling rate. Such a large microstructure for GC samples could cause reductions in their mechanical properties.[14] Note that the number of repetition for this measurement is more than 100.

B. Tensile Properties

Figure 4 shows the tensile properties of the VC samples created at different casting speeds: (a) ultimate tensile strength σ_{UTS}, (b) 0.2 pct proof strength $\sigma_{0.2}$, and (c) fracture strain ε_{f}. It is obvious that the data points are widely scattered and that there is no clear correlation between tensile properties and casting speed. The average tensile properties with their standard deviation values are summarized in Table II. Since the tensile properties are similarly observed for all casting conditions, there would be no clear casting speed effects on the material properties (for CS = 400 to 1300 mm/s). In the previous works, opposite experimental results were reported, where the lower defect rate in cast aluminum alloys was made by the vacuum pressure casting, leading to the higher mechanical properties.[17,18] Such difference might be attributed to the different casting speeds, where our casting speed would be much higher than that for the other ones. Because turbulent flow occurs for our all VC samples during the casting process at 400, 700, 1000, and 1300 mm/s, similar defect rate (or similar mechanical properties) would be obtained: Reynolds number (Re) for all casting speed calculated is more

than 2000, *e.g.*, $Re = \text{CS} \times d/v$, where d is diameter of the mold and v is viscosity. In this case, Re for the casting speed 400 mm/s is found to be 12,000, which is much higher than that for 2000, *e.g.*, $Re = 400$ mm/s (CS) × 6 mm (d)/0.2 mm^2/s (v). The mean tensile strength of the VC samples was about 250 MPa, which is almost equal to that for the conventional die-cast Al
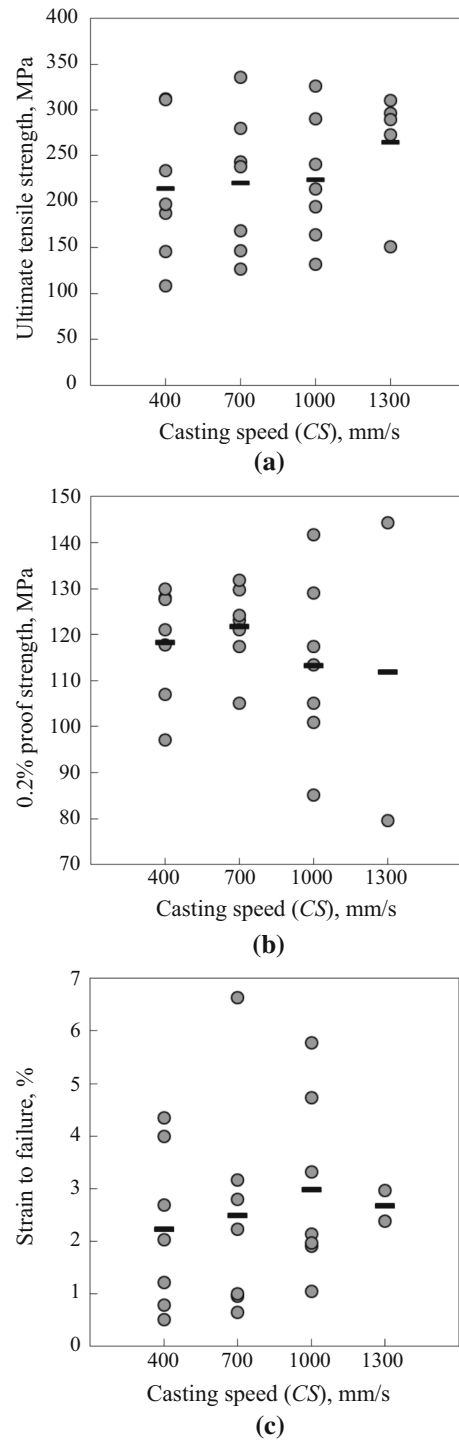

Fig. 4—Relationship between tensile properties and casting speed for the VC samples: (a) ultimate tensile strength σ_{UTS}, (b) 0.2 pct proof strength $\sigma_{0.2}$, and (c) fracture strain ε_{f}.

Table II. Data Analysis of the Tensile Properties of the VC Samples: σ_{UTS}, $\sigma_{0.2}$, and ε_f

| Casting Speed	400 mm/s	700 mm/s	1000 mm/s	1300 mm/s
Ultimate tensile strength (σ_{UTS}) (MPa)				
Average σ_{UTS}	213.9 MPa	219.8 MPa	222.9 MPa	264.2 MPa
Standard deviation	77.7 MPa	75.9 MPa	68.4 MPa	64.6 MPa
0.2 pct proof strength ($\sigma_{0.2}$) (MPa)				
Average $\sigma_{0.2}$	118.3 MPa	121.7 MPa	113.2 MPa	119.9 MPa
Standard deviation	12.2 MPa	8.8 MPa	18.6 MPa	45.7 MPa
Strain to failure (ε_f) (pct)				
Average ε_f	2.22 pct	2.48 pct	2.98 pct	2.67 pct
Standard deviation	1.52 pct	2.07 pct	1.71 pct	0.41 pct
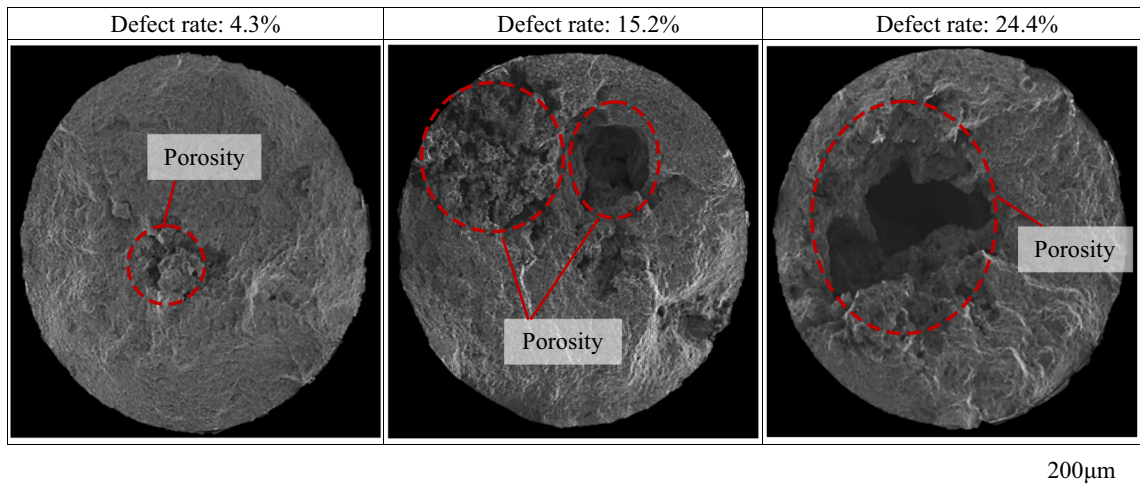
Fig. 5—SEM images for the VC samples showing the porosity on the fracture surface after tensile tests.

alloy (ADC12), 240 MPa.[19] Because of the similar microstructural characteristics in all VC samples (SDAS and size of the eutectic phase), as mentioned above, the scattered data and weak correlation could be attributed to other factors such as cast defects.

Figure 5 displays scanning electron microscopy (SEM) images of the fracture surfaces of representative VC specimens after tensile tests. As can be observed, different amounts of cast defects (porosity) can be obtained, although this volume fraction was dependent on the sample. Note that other defects, such as shrinkage and inclusion, cannot be detected on the fracture surfaces. As seen, the shape of porosity is complicated in the specimen and those are located randomly. Figure 6 shows the relationship between casting speed and the area fraction of the porosity on the fracture surface, namely the defect rate (DR). In this case, the area fraction of the porosity was measured on the fracture surface using an image analyzer. This is because the tensile properties of the related Al alloys are correlated with their area fraction of defect in the fracture surface.[12] As seen in Figure 6(a), no clear correlation between the DR and casting speed was detected. Moreover, Figure 6(b) shows the area fraction of each porosity on the facture surface for the VC samples, where more than 25 porosities were measured. From this, different pore sizes are detected with wide range for all casting speed conditions. The reason for

this can be interpreted by their turbulent flows as mentioned above. The reason behind this is not clear at the moment, but it will be investigated in the future. Figure 7 shows stress–strain curves for representative samples with different DRs, where the tensile properties appear to be influenced by the amount of cast defect, *i.e.*, the higher the tensile strength, the lower the DR.

Figure 8 shows tensile properties *vs* DR. As can be seen in Figures 8(a) and (b), almost linear correlations are detected between the ultimate tensile strength (σ_{UTS}) and DR and the 0.2 pct proof strength ($\sigma_{0.2}$) and DR: $\sigma_{UTS} = -5.4DR + 313.3$ ($R^2 = 0.64$) and $\sigma_{0.2} = l0.83DR + 130.8$ ($R^2 = 0.30$). Those equations were estimated using data analysis software (Origin 2015), where we have selected suitable equations with high R^2 value. It should be pointed out that, in this case, the data plots are relatively scattered due to the low correlation rates. The reason for this is not clear at the moment, but this could be affected by the complicated defect characteristics, *e.g.*, pore shape, location, and size (Figures 5 and 6(b)). In the previous work, a similar relationship between tensile strength (σ_{UTS} and $\sigma_{0.2}$) and porosity in the proximity of the fracture in aluminum alloys was reported, although the evaluation was only conducted at low porosity rates of less than 3 pct;[7] moreover, Nakata *et al.*[20] have reported the effect of cast defect (cold flake) on the tensile properties, and the tensile strength is relatively scattered. This would be attributed
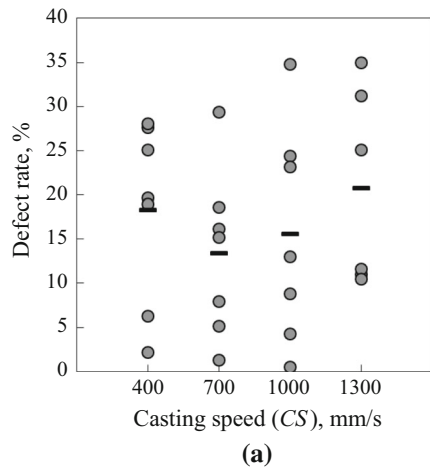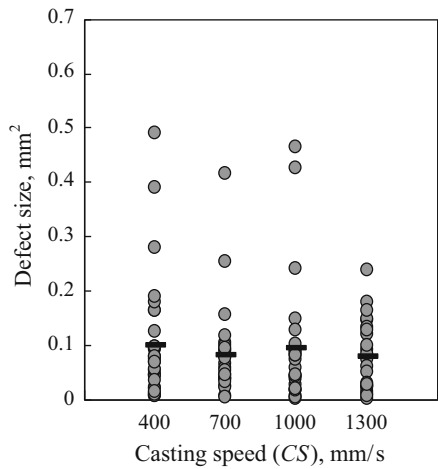
Fig. 6—(a) Relationship between the casting speed and the area fraction of the porosity on the fracture surface for the VC samples. (b) Porosity size of the VC samples.
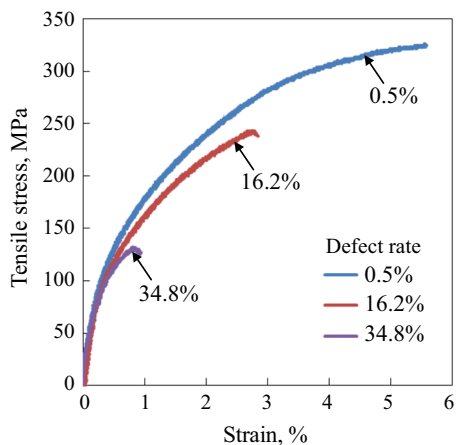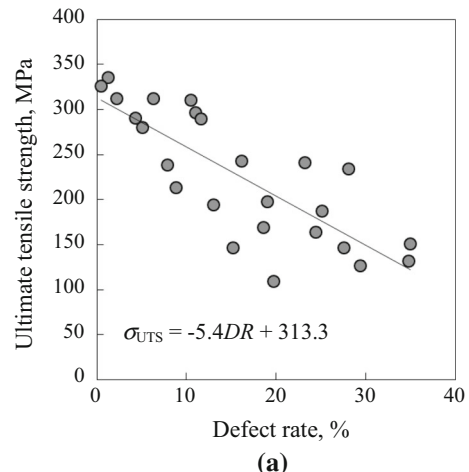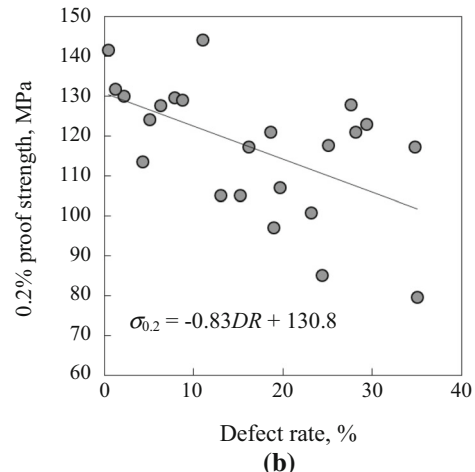

Fig. 7—Representative tensile stress *vs* tensile strain curves for the VC samples.

Fig. 8—Relationship between the tensile properties and the area fraction of the porosity on the fracture surface (DR) for the VC samples: (a) ultimate tensile strength, (b) 0.2 pct proof strength, and (c) fracture strain.
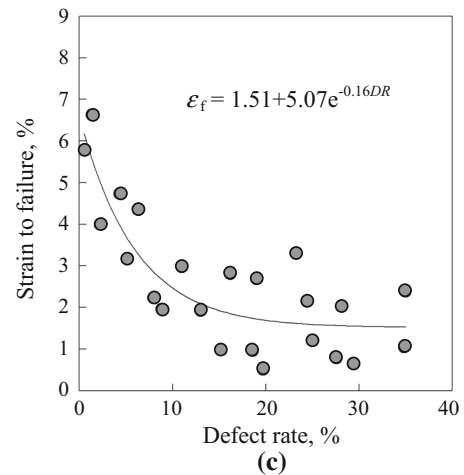
to the complicated structure of cold flake. On the contrary, in Figure 8(c), a non-linear relationship was obtained for fracture strain (ε_f) *vs* DR: $\varepsilon_f = 1.5 + 5.1\,e^{-0.16DR}$ ($R^2 = 0.73$). The strain value dropped rapidly

to approximately 2 pct, even if there was only a small amount of defect in the cast sample, *e.g.*, DR < 5 pct, and the strain level became almost constant for samples with DR > 10 pct. Such a non-linear relation was also detected in a previous study by Welter and Wood,[10] in which the empirical relationship between the fracture

strain and the area fraction of porosity was approximated as $\varepsilon_f = 0.016f^{-0.30}$.[10] Note that the coefficient of the formula in Welter and Wood[10] is slightly different to ours in Figure 8(c), which might be because of the different material properties. It is concluded from this result that the low amount of porosity is extremely sensitive to the fracture strain. To verify the above tensile properties, a further approach was conducted using specimens with artificial defects.

Figure 9 presents representative tensile stress–tensile strain curves for the HMC and GC samples with artificial defects of different sizes. As can be seen, different tensile properties are evident, with the stress vs strain for HMC and for GC samples with high DR (or large defect size) indicating lower tensile properties. The overall tensile properties for HMC samples are higher than those for GC samples. Interestingly, the stress–strain curves for the samples of 0.1 mm in diameter almost overlap with the curves for the samples without defects, where there are no strong defect effects on the tensile properties. The reason behind this is not clear at the moment but this may be attributed to the following reason. In our cast aluminum alloy, there would have two main factors to affect the mechanical
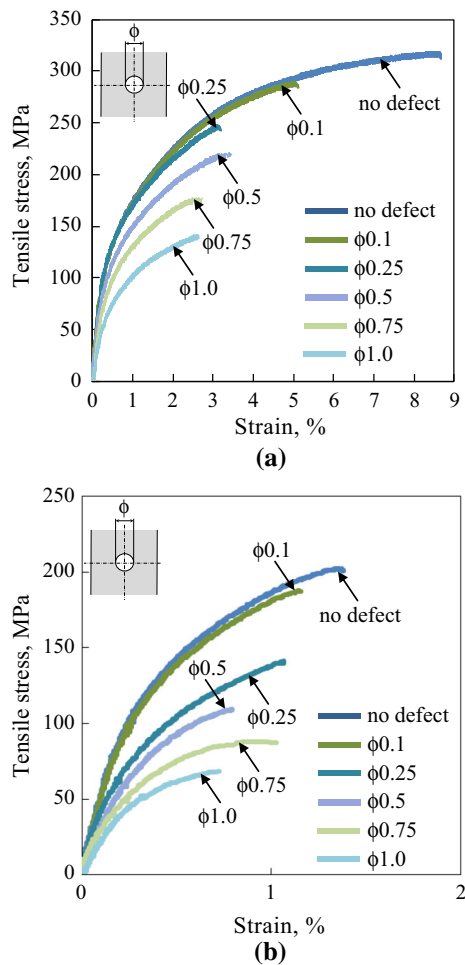
properties, $e.g.$, defects and microstructures. The later one could be influenced due to the needle-shaped hard Si or Fe based eutectic structures, whose stress concentrations should be high value compared to that for the artificial defect (hole of 0.1 mm in diameter). However, further study will be required in the future.

Figure 10 shows the variation of the tensile properties as a function of the artificial defect rate (DR_A): (a) ultimate tensile strength (σ_{UTS}), (b) 0.2 pct proof strength ($\sigma_{0.2}$), and (c) fracture strain (ε_f). In this case,

Fig. 9—Representative tensile stress vs tensile strain curves for (a) HMC and (b) GC samples with single artificial defects.
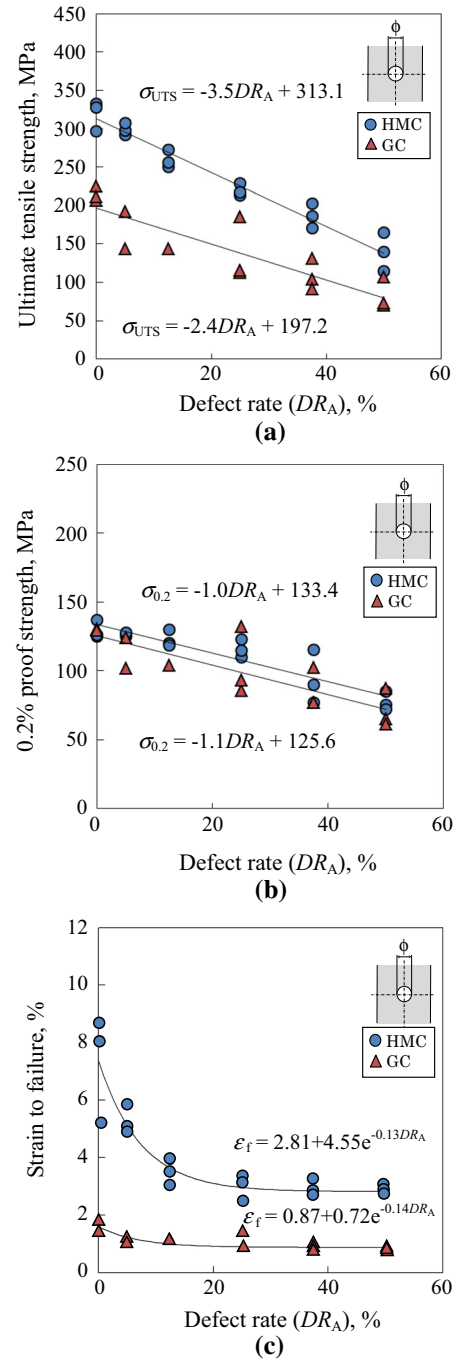
Fig. 10—Variation of tensile properties as a function of artificial defect rate (DR_A) for the HMC and GC samples: (a) ultimate tensile strength, (b) 0.2 pct proof strength, and (c) fracture strain.

DR$_A$ is defined as the area fraction of the machined hole on the fracture surface, which is the same evaluation for cast porosity (DR in Figure 8). It is clear that there are linear correlations between the tensile properties (σ_{UTS} and $\sigma_{0.2}$) and the area fractions of the artificial defects (DR$_A$) ($\sigma_{UTS} = -3.5$DR$_A + 313.1$ for HMC samples and $\sigma_{UTS} = -2.4$DR$_A + 197.2$ for GC samples; $\sigma_{0.2} = -1.0$DR$_A + 133.4$ for HMC samples and $\sigma_{0.2} = -1.1$DR$_A + 125.6$ for GC samples). Higher σ_{UTS} values were obtained for HMC samples compared to GC samples. The ultimate tensile strength can be affected by the different sizes of the microstructures. The linear variations for σ_{UTS} and $\sigma_{0.2}$ are similar to those for VC samples (see Figure 8). However, the reduction rates of the tensile strength for VC samples (Figure 8(a)) are obviously high compared to the HMC and GC samples. This could be because of the complicated defect formation for VC samples, as shown in the SEM images. It should be pointed out that the variation of $\sigma_{0.2}$ was similarly obtained for HMC and GC samples. This may have been caused by a weak microstructural effect on their $\sigma_{0.2}$ values. In addition, similar $\sigma_{0.2}$ values were obtained for both samples with DR$_A < 20$ pct, which led to a weak attribution to their $\sigma_{0.2}$ values. Like the results for VC samples, a non-linear relationship was obtained between ε_f and DR$_A$ for HMC and GC samples, in which $\varepsilon_f = 2.8 + e^{-1.13\text{DRA}}$ ($R^2 = 0.86$) for HMC and $\varepsilon_f = 0.87 + 0.72e^{-0.14\text{DRA}}$ ($R^2 = 0.73$) for GC. The higher coefficient of the empirical formula for GC samples could be caused by the significantly bigger microstructure, e.g., high stress concentration arising from brittle eutectic structures, as shown in Figure 3. The above tensile properties will be further discussed in section III-C.

A further approach was carried out using the HMC and GC samples with numerous artificial defects (ϕ 0.25 mm). In this case, the defects were made at perpendicular (90 deg), 45 deg, and parallel (0 deg) directions against the loading direction (see Figure 1). The representative stress–strain curves for the samples with 90 deg defects are presented in Figure 11. Similar to the results of Figure 10, clear correlations between the tensile properties and DR can be seen. The obtained tensile properties (σ_{UTS} and ε_f) are summarized in Figure 12. Note that in this case, the DR was evaluated by the volume fraction of the specimen. It can be seen that a significant reduction in the tensile properties was obtained for samples with artificial defects (DR$_V$) with 0 and 45 deg directions compared to those for the sample with a 90 deg direction (Figure 12(a–iii)). Such severe reductions in the tensile properties for 0 and 45 deg samples were caused by the high stress concentrations of their artificial defects. On the other hand, the weak defect effects for the samples with defects of 90 deg direction could be because of the low area fraction of the defect to the loading direction. Moreover, a low tensile strength could be observed for the GC samples, which is caused by the microstructures. Similar to the single defect specimen, non-linear ε_f vs DR$_V$ curves are obtained for the multiple defects shown in Figure 12(b), and the low ε_f variation can be seen for the GC samples. From the above results, it can be
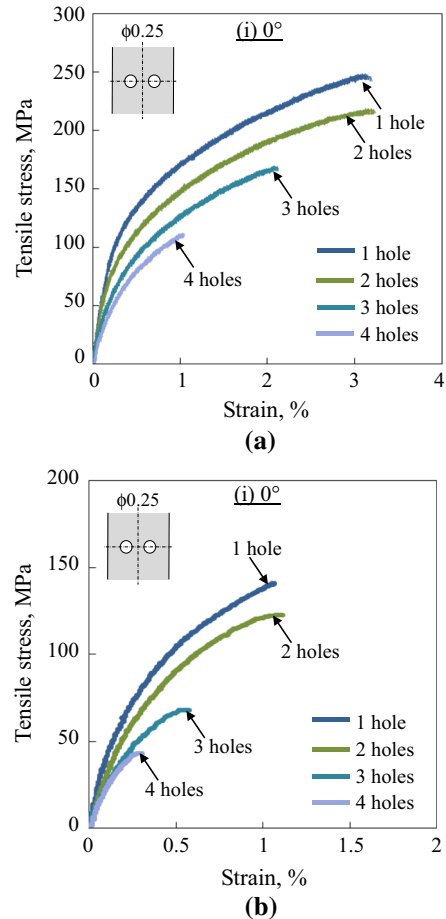

Fig. 11—Representative tensile stress *vs* tensile strain curves of (*a*) HMC and (*b*) GC samples with 0 deg defects.

summarized briefly that the tensile properties are directly affected by the amount of defects, as well as their position and the size of the microstructure.

C. Strain Characteristics

To examine the failure characteristics of the HMC and GC samples during tensile tests, strain observation was conducted directly using a Correlation System VIC-2D with high-speed cameras. Figure 13 presents the strain distribution (Y axis) of the HMC and GC samples with artificial defects of ϕ0.1 mm and ϕ 0.25 mm. In this case, the strain distribution was observed at several loading points. It can be seen that in the HMC sample with ϕ0.1 mm and ϕ0.25 mm defects, there are relatively uniform strain distributions in the specimens during the loading process, although the strain level increases and the high strain values are concentrated around the artificial defects just before the final failure. Uniform strain distributions at the yield point were similarly obtained for the HMC and GC samples, which led to a similar 0.2 pct proof strength between GC and HMC samples (Figure 10(b)). After the yield point, the strain levels increased rapidly in some localized areas in the GC samples, in which the
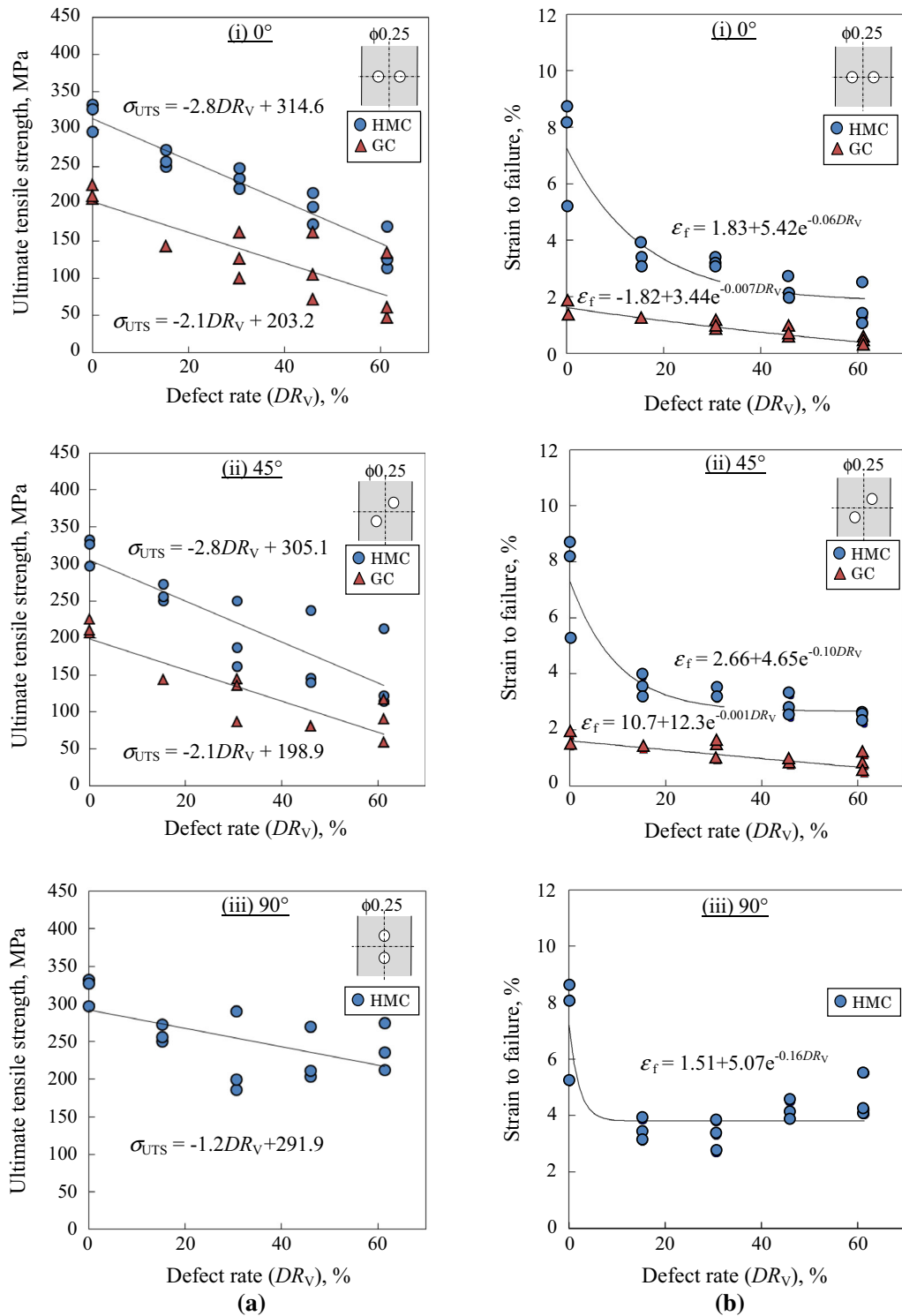
Fig. 12—Variation of tensile properties as a function of artificial defect rate (DR$_V$) for the HMC and GC samples: (*a*) ultimate tensile strength and (*b*) fracture strain.

high strain was not only located around the defects but also elsewhere in the specimens. Because there were large eutectic phases (needle-shaped Si and Fe structures) and grain boundaries in GC samples, these structures were able to create a localized strain distribution. In fact, in some associated samples, cracks did not grow through the artificial defect of ϕ0.25 mm for GC samples (see Figure 13(d)). One of the present authors has examined the hardness of eutectic structures in ADC12 aluminum alloys using an ultra-microhardness tester, in which high Martens hardness value of 6.36 GPa for the Al-Fe-based eutectic structures,[15]
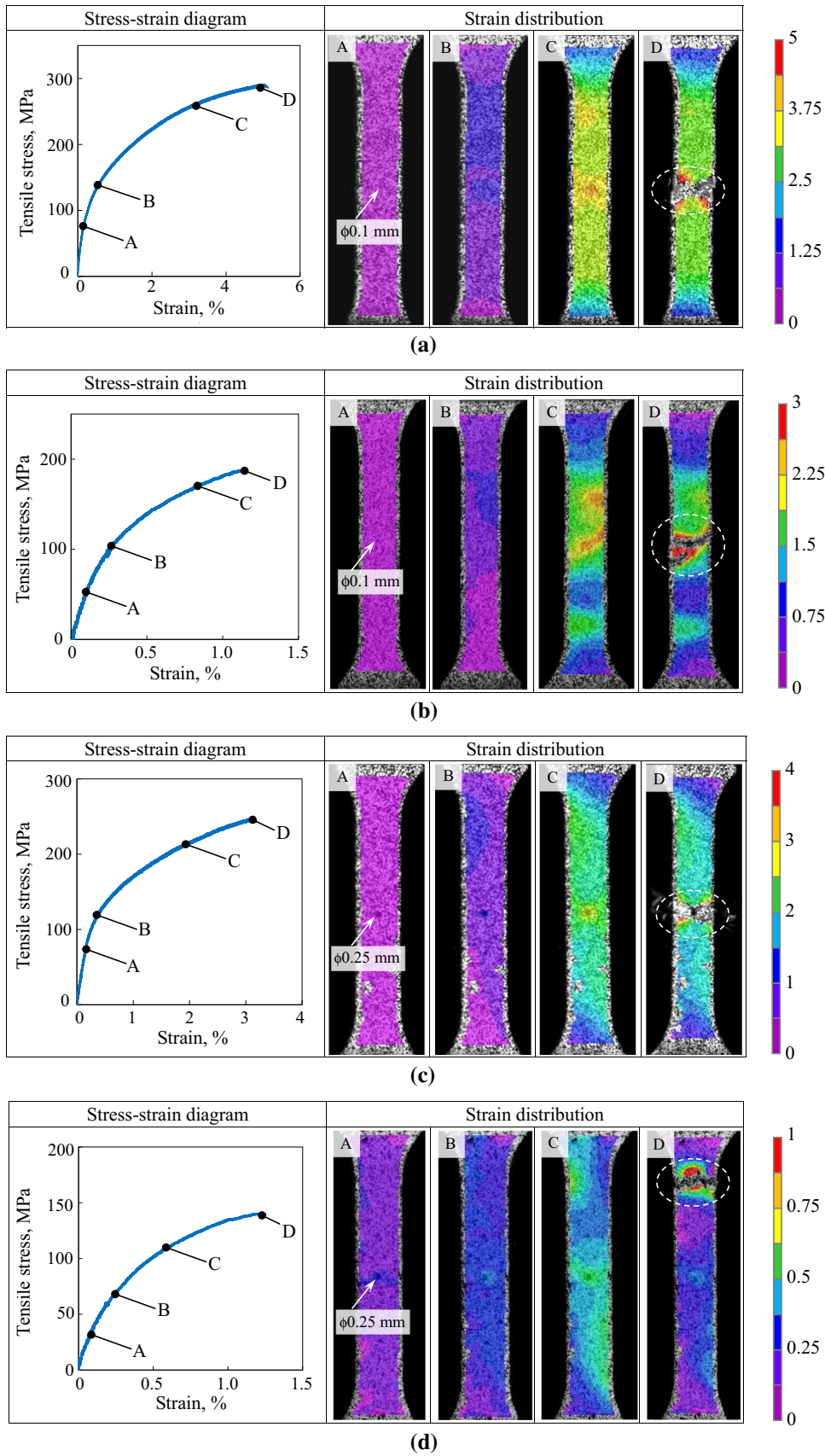
Fig. 13—Strain distribution (Y axis) in the HMC and GC samples with single artificial defects (ϕ0.1 mm and ϕ0.25 mm) during tensile loading.

which are about 8 times higher than the hardness of the α-Al phase (0.8 GPa). To verify this, direct observation of the fracture surfaces was conducted. Figure 14 displays SEM micrographs of the fracture surfaces for the HMC and GC samples with single artificial defect of ϕ0.25 mm. From this observation, Fe element arising from the related eutectic strictures is distributed in large area of the fracture surface for the GC sample, while no clear Fe element for the HMC one. Such Fe-base structures make high stress concentration; and this could make a weak effect of the artificial defect on the fracture mode.

Figure 15 shows the strain distribution (Y axis) of the HMC samples with multiple artificial defects of ϕ 0.25 mm just before the fracture was examined experimentally and numerically, *i.e.*, at 0, 45, and 90 deg directions. Although the strain distribution was altered because of the different defect directions, high strain regions can be observed in the samples around the artificial defects. These strain distributions were verified by FE analysis, where the plastic strain distribution in the HMC samples is indicated (see Figure 15). The high strain levels are distributed in the specimen adjacent to the artificial defects in all samples. Such strain distributions approximately correspond to the experimentally obtained strain characteristics. From this, it can be considered that our numerical analysis (or the FE analysis parameters in Table I) conducts accurate stress-strain analysis for related cast Al alloys.
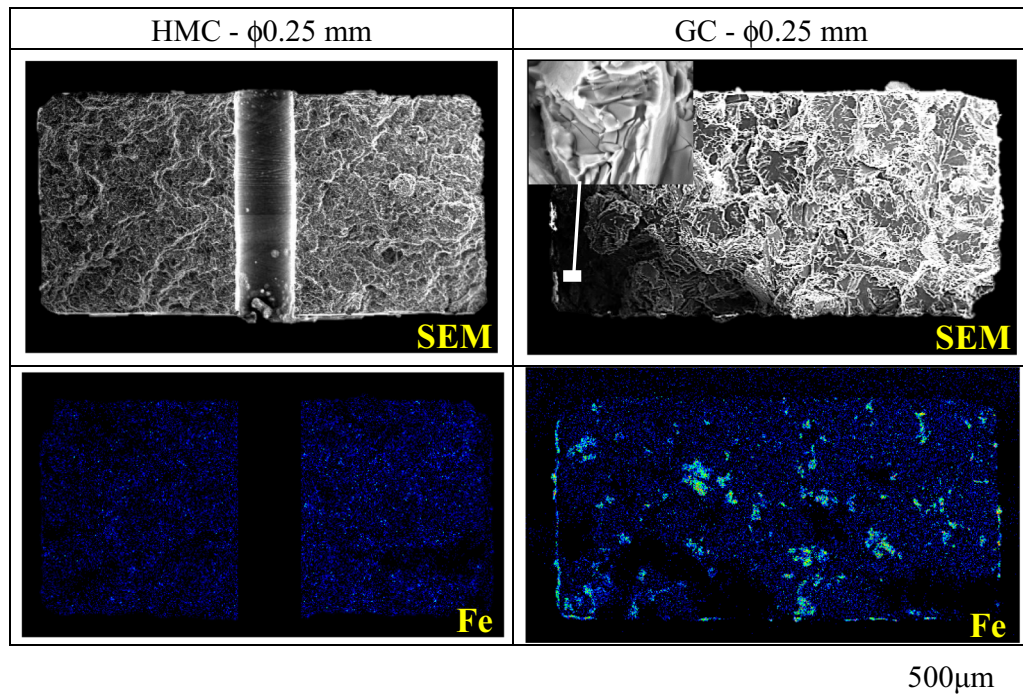

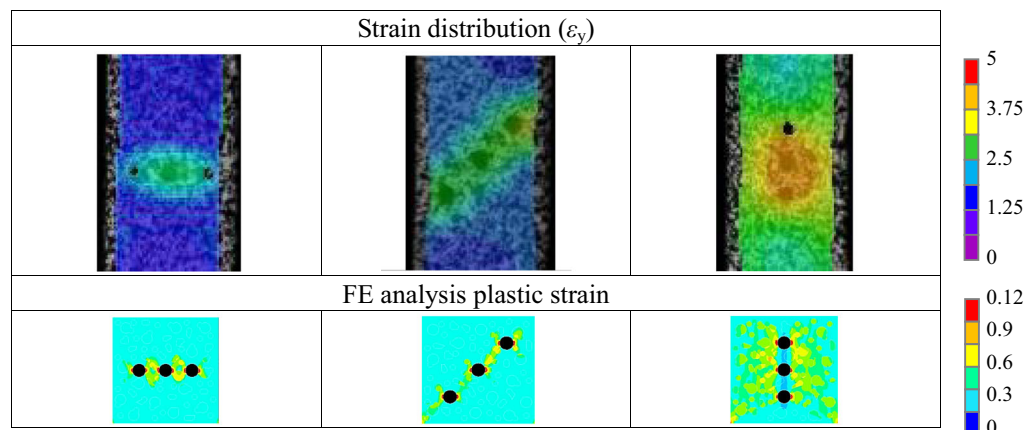Fig. 14—Fracture surfaces for the HMC and GC samples with single artificial defects (ϕ0.25 mm).

Fig. 15—Strain distribution (Y axis) examined experimentally and numerically in the HMC samples with multiple artificial defects at just before fracture.

IV. CONCLUSIONS

The effects of cast defects on the mechanical properties of cast ADC12 Al alloys have been studied. On the basis of the results obtained, the following conclusions can be drawn:

1. Linear correlations were detected between the DR and ultimate tensile strength, as well as the DR and 0.2 pct proof strength. On the contrary, a non-linear relationship was obtained for DR *vs* fracture strain. The fracture strain dropped rapidly to approximately 2 pct, even if small amounts of defect were involved (*e.g.*, DR < 5 pct), and the strain level became almost constant for the sample with DR > 10 pct. The tensile properties were strongly attributed to the area fraction of defect in the fracture surface.
2. Tensile properties were investigated using HMC and GC samples with numerous artificial defects (ϕ 0.25 mm), where the defects were created on specimens with 0, 45, and 90 deg directions against the loading direction. Although linear correlations between the DR_A and tensile properties (σ_{UTS} and $\sigma_{0.2}$) were obtained clearly for all cast aluminum alloy, significant reduction in the tensile properties was obtained for the samples with the defects of 0 and 45 deg because of the high stress concentration. It also appeared that the area fraction of the defect to the loading direction was a significant factor for determining the tensile properties.
3. There was a weak defect effect on the tensile properties of the cast Al alloy, because the DR was less than 5 pct, where the stress *vs* strain curves for the Al alloy with 5 pct defects almost overlapped with the curves for samples without defects. A small amount of defect (<20 pct) and the microstructural characteristics do not strongly affect the $\sigma_{0.2}$ value of the cast aluminum alloy.
4. Strain characteristics were clarified experimentally and numerically. A high strain distribution was detected around the defects just before the final fracture point for HMC samples, and such high strain levels were seen in both the eutectic phases and the defects for GC samples. However, localized severe strains were not detected around the defects and the eutectic phase at the yield point, resulting in a similar 0.2 pct proof strength.

REFERENCES

1. M.A. Irfan, D. Schwam, A. Karve, and R. Ryder: *Mater. Sci. Eng. A*, 2012, vol. 535, pp. 108–14.
2. C.H. Caceres: *Metall. Mater. Trans A*, 2007, vol. 38A, pp. 1649–61.
3. H.R. Ammar, A.M. Samuel, and F.H. Samuel: *Int. J. Fatigue*, 2008, vol. 30, pp. 1024–35.
4. O. Kuwazuru, Y. Murata, Y. Hangai, T. Utsunomiya, S. Kitahara, and N. Yoshikawa: *J. Solid Mech. Mater. Eng.*, 2008, vol. 9, pp. 1220–31.
5. A.K.M. Aziz and H. Ahamed: *Mater. Trans. JIM*, 2008, vol. 49, pp. 1621–28.
6. S. Jana, R.S. Mishra, J.B. Baumann, and G. Grant: *Acta Mater.*, 2010, vol. 58, pp. 989–1003.
7. G.W. Mugica, D.O. Tovio, J.C. Cuyas, and A.C. Conzátes: *Mater. Res.*, 2004, vol. 7, pp. 221–29.
8. H.D. Zhao, F. Wang, Y.Y. Li, and W. Xia: *J. Mater. Process. Technol.*, 2009, vol. 209, pp. 4537–42.
9. C. Kawai and A. Yamakawa: *J. Am. Ceram. Soc.*, 1997, vol. 80, pp. 2705–08.
10. J.P. Weiler and J.T. Wood: *Mater. Sci. Eng. A*, 2009, vol. 527, pp. 32–37.
11. J.P. Weiler and J.T. Wood: *Mater. Sci. Eng. A*, 2009, vol. 527, pp. 25–31.
12. C.H. Cáceres and B.I. Selling: *Mater. Sci. Eng. A*, 1996, vol. 220, pp. 109–16.
13. M. Avalle, G. Belingardi, M.P. Cavatorta, and R. Doglione: *Int. J. Fatigue*, 2002, vol. 24, pp. 1–9.
14. M. Okayasu, S. Takeuchi, M. Yamamoto, and H. Ohfuji: *Metall. Mater. Trans A*, 2015, vol. 46A, pp. 1597–1609.
15. M. Okayasu, S. Takasu, and M. Mizuno: *J. Mater. Sci.*, 2012, vol. 47, pp. 241–50.
16. W.C. Oliver and G.M. Pharr: *J. Mater. Res.*, 2004, vol. 19, pp. 3–20.
17. A. Ueno, S. Miyakawa, K. Yamada, and T. Sugiyama: *Proc. Eng.*, 2010, vol. 2, pp. 1937–43.
18. Q. Yan, H. Yu, Z. Xu, B. Xiong, and C. Cai: *J. Alloy. Compd.*, 2010, vol. 501, pp. 352–57.
19. M. Okayasu, Y. Ohkura, S. Takeuchi, S. Takasu, H. Ohfuji, and T. Shiraishi: *Mater. Sci. Eng. A*, 2012, vol. 543, pp. 185–92.
20. N. Nakata, Y.G. Kim, H. Fujii, T. Tsumura, and T. Komazaki: *Mater. Sci. Eng. A*, 2006, vol. 437, pp. 274–80.